Non-storm erosion of MeV electron outer radiation belt down to *L** < 4.0 associated with successive enhancements of solar wind density

Ying Xiong[1,2], Lun Xie[1]*, SuiYan Fu[1]*, BinBin Ni[3], and ZuYin Pu[1]

[1]School of Earth and Space Science, Peking University, Beijing 100871, China;

[2]Department of Earth and Space Sciences, Southern University of Science and Technology, Shenzhen 518055, China;

[3]Department of Space Physics, School of Electronic Information, Wuhan University, Wuhan 430072, China

Key Points:
- The non-storm loss mechanisms of MeV electrons in the outer radiation belt during three successive solar wind density enhancements are investigated.
- The losses of electrons with small pitch angles are first controlled by outward radial diffusion at *L** > 4, then by EMIC-wave-driven pitch angle scattering at 4 < *L** < 5.
- Outward radial diffusion is the primary loss mechanism for large pitch angle electrons.

Abstract: We report an unusual non-storm erosion event of outer zone MeV electron distribution during three successive solar wind number density enhancements (SWDEs) on November 27−30, 2015. Loss of MeV electrons and energy-dependent narrowing of electron pitch angle distributions (PAD) first developed at *L** = 5.5 and then moved down to *L** < 4. According to the evolution of the electron phase space density (PSD) profile, losses of electrons with small pitch angles at *L** > 4 during SWDE1 are mainly due to outward radial diffusion. However during SWDE2&3, scattering loss due to EMIC waves is dominant at 4 < *L** < 5. As for electrons with large pitch angles, outward radial diffusion is the primary loss mechanism throughout all SWDEs which is consistent with the incursion of the Last Closed Drift Shell (LCDS). The inner edge of EMIC wave activity moved from *L** ~5 to *L** ~4 and from *L* ~6.4 to *L* ~4.2 from SWDE1 to SWDE2&3, respectively, observed by Van Allen Probes and by ground stations. This is consistent with the inward penetration of anisotropic energetic protons from *L** = 4.5 to *L** = 3.5, suggesting that the inward extension of EMIC waves may be driven by the inward injection of anisotropic energetic protons from the dense plasma sheet.

Keywords: solar wind density enhancement; outer radiation belt; MeV electrons; outward radial diffusion; EMIC wave scattering loss

1. Introduction

Recent studies have shown that outer belt electrons can also exhibit dramatic losses (Morley et al., 2010; Ni BB et al., 2013; Su ZP et al., 2014, 2016; Katsavrias et al., 2015; Engebretson et al., 2018; Tu WC et al., 2019, Ma X et al., 2020) and accelerations (Su ZP et al., 2015) during non-storm periods. Losses of MeV electrons can be attributed to either adiabatic processes (the *Dst* effect during enhancement of the ring current (Kim and Chan, 1997) or non-adiabatic processes. The non-adiabatic loss processes can be divided into two major categories: (1) magnetopause incursion due to sudden compression of the magnetopause in combination with subsequent outward radial transport (Shprits et al., 2006;

Loto'aniu et al., 2006; Turner et al., 2012; Hudson et al., 2014; Xiang Z et al., 2017, 2018), and (2) precipitation into the atmosphere driven by chorus waves (Lorentzen et al., 2001; Breneman et al., 2017; Mozer et al., 2017), hiss waves (Meredith et al., 2004; Millan and Thorne, 2007), and especially by EMIC waves which can lead to the efficient loss of MeV electrons (Summers and Thorne, 2003; Li W et al., 2007; Su ZP et al., 2011; Kersten et al., 2014; Usanova et al., 2014; Aseev et al., 2017). During the main phase of a geomagnetic storm, non-adiabatic loss processes coincide with adiabatic processes, and thus it is difficult to evaluate the actual electron loss due to non-adiabatic processes alone. Non-storm electron loss events, of which relatively few events have been studied, provide us excellent opportunities to investigate the relative importance of the two major non-adiabatic loss mechanisms and their connections to solar wind drivers.

It is well known that the flux of outer zone relativistic electrons positively correlates with the solar wind speed (Blake et al., 1997; Li XL et al., 2001; Reeves et al., 2011; Borovsky and Denton, 2014).

Meanwhile, recent statistical results suggest that the solar wind density plays an important role in the dynamics of outer belt electrons and sometimes controls the major variations of relativistic electron fluxes (Lyatsky and Khazanov, 2008; Balikhin et al., 2011; Boynton et al., 2013; Xiong Y et al., 2015). A negative correlation between the solar wind density and relativistic electron fluxes at geosynchronous orbit (Lyatsky and Khazanov, 2008) and outer radiation belt electron content (Xiong Y et al., 2015) has been confirmed. The strong connection between the solar wind density and outer belt electron fluxes is relatively unexpected since density is not a key factor for the generation of geomagnetic activity (Lyatsky and Khazanov, 2007). Two major hypotheses have been proposed to explain why high solar wind density can result in low electron flux in the outer radiation belt. One is that high solar wind density can lead to the enhancement of the solar wind dynamic pressure resulting in electron losses via the "magnetopause shadowing" effect (Loto'aniu et al., 2006). The other is that the enhanced solar wind can lead to a superdense plasma sheet (Borovsky et al., 1998); the overlap of the super dense and hot plasma sheet and cold plasmasphere/plasmaspheric plumes can provide favorable conditions for the excitation of electromagnetic ion cyclotron (EMIC) waves (Borovsky and Denton, 2009; Chen LJ et al., 2010). Enhanced EMIC wave activity can then cause electron scattering loss into the atmosphere, especially for MeV electrons (Summers and Thorne, 2003). However, both hypotheses have rarely been evaluated in a manner of case analysis. Wang DD et al. (2020) analyzed a non-storm loss event during which the enhanced solar wind density and dynamic pressure were observed. They suggested that the magnetopause incursion due to enhanced solar wind dynamic pressure and subsequent outward radial diffusion can account for the electron loss. Therefore, aside from EMIC wave scattering loss, magnetopause shadowing and outward radial diffusion are also important contributors to electron loss during enhanced solar wind density periods. A detailed case study of the primary process responsible for outer radiation belt electron loss during intervals of high solar wind density is urgently needed. Besides, the enhancement of solar wind density can also naturally cause the enhancement in dynamic pressure, which controls the spatiotemporal distribution of EMIC waves (Anderson and Hamilton, 1993; Engebretson et al., 2002; Usanova et al., 2008; Liu NG et al., 2020) and then impacts the loss of relativistic electrons in the outer radiation belt. Thus, it is quite challenging to exclude the influence of enhanced solar wind dynamic pressure when evaluating the impacts of enhanced solar wind density on outer belt electron loss.

In this paper, we report an unusual non-storm outer radiation belt erosion event during three prolonged consecutive enhancements of solar wind density on 27–30 November 2015. By investigating the evolution of electron pitch angle distribution (PAD) and phase space density (PSD) obtained from the twin Van Allen Probes, and the features of EMIC wave activity observed by Van Allen Probes and ground stations, we attempt to reasonably determine the dominant loss mechanism for this non-storm outer zone electron erosion event.

2. Data
The energetic electron and low-energy proton flux data used in

this work are obtained from the Magnetic Electron Ion Spectrometer (MagEIS) (Blake et al., 2013), Relativistic Electron-Proton Telescope (REPT) (Baker et al., 2013), and the Helium Oxygen Proton Electron (HOPE) mass spectrometer (Funsten et al., 2013) aboard Van Allen Probes (Mauk et al., 2013). The adiabatic invariants calculated with the TS04 magnetic field model are obtained from the Magnetic Ephemeris database (https://www.rbspect.lanl.gov/data_pub/). The high time-resolution magnetic field data used to obtain the EMIC wave spectrum distribution are obtained by the Electric and Magnetic Field Instrument Suite and Integrated Science (EMFISIS) (Kletzing et al., 2013). Magnetometer data with an 8 samples/s cadence measured by ground-based stations at different latitudes (the Canadian Array for Realtime Investigations of Magnetic Activity, CARISMA, www.carisma.ca) are used to monitor the EMIC wave activity at different L-shells. The Medium Energy Proton and Electron Detector instrument (MEPED) (Evans and Greer, 2004; Green, 2013) aboard three Polar-orbiting Operational Environmental Satellite (POES)/NOAA satellites (NOAA-15, NOAA-18, and Metop-01) are used for investigating electron precipitations. Solar wind parameters and geomagnetic indices used in this paper are obtained from the SFC/SPED OMNI-Web interface at http://omniweb.gsfc.nasa.gov.

3. Observations

3.1 Non-storm Erosion of MeV Electrons in the Outer Radiation Belt

A non-storm MeV electron loss event was measured by the twin Van Allen Probes during three enhancements of solar wind density on 27–30 November 2015. The Kp index during this period reached up to 3 and 4, which means that geomagnetic conditions were not quiet and "geospace storms" occurred (Borovsky and Shprits, 2017). However, in this paper, we use the term "non-storm" to represent the condition of no evident enhancements of ring current, where the Dst index is close to 0 nT. During the first solar wind density enhancement (SWDE1, marked by the blue bar at the top of Figure 1), the spin-average flux of 2.1 MeV electrons presented an evident decrease from $L^* = 5.5$ down to $L^* = 4.5$. Next, the loss of electrons evolved down to a lower L-shell ($L^* \sim 4.0$) at the end of the second solar wind density enhancement (SWDE2, denoted by the green bar). The decrease of the 2.1 MeV electron flux was observed below $L^* = 4$ at the end of the third solar wind density enhancement (SWDE3, denoted by the red bar). Figure 1a shows the Last Closed Drift Shell (LCDS) of electrons with $K = 0.4$ $G^{1/2}R_E$ obtained from the LANLGeoMag library using the TS04 magnetic field model. There are notable incursions of LCDS during the three SWDEs and the inward motions are roughly consistent with the 2.1 MeV electron loss at the apogee of the Van Allen Probes orbit, suggesting that magnetopause incursion and outward radial diffusion contributed to the loss at high L-shells. Figure 1c illustrates the orbit plot of the exponential index n (the fitting coefficient of 2.1 MeV electron PAD using $\sin^n\alpha$) (Vampola, 1998). The n-index remained nearly constant at different L-shells before SWDE1. It then increased rapidly, indicating that the PAD of 2.1 MeV electrons became narrowed, along with a decrease in the electron flux from $L^* = 5.5$ down to $L^* < 4$. Fluxes of >2 MeV electron measured by GOES-13 (blue line) and GOES-15
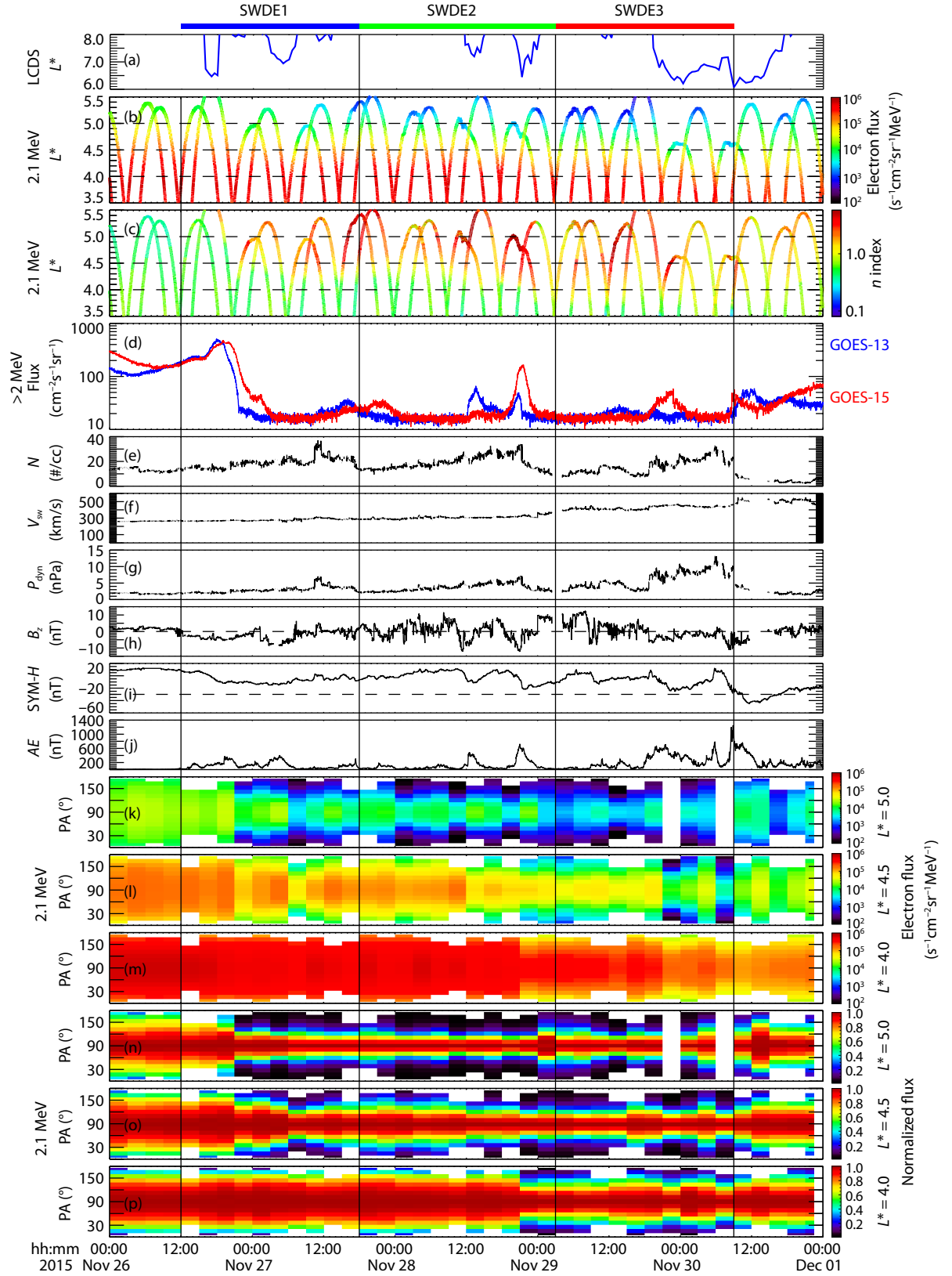
Figure 1. Overview of the outer zone MeV electron erosion event on November 27–30, 2015. (a) the Last Closed Drift Shell (LCDS) of electrons with $K = 0.4\ G^{1/2}R_E$; (b) 2.1 MeV electron flux measured by Van Allen Probes A and B; (c) the fitting coefficient of the 2.1 MeV electron PAD using $\sin^n \alpha$; (d) the electron flux with energy greater than 2 MeV measured by GOES-13 (blue trace) and GOES-15 (red trace); (e–j) solar wind density, speed, dynamic pressure, IMF B_z, SYM-H index and AE index; (k–m) the 2.1 MeV electron PADs at $L^* = 5$, 4.5 and 4, respectively; (n–p) the normalized PADs of 2.1 MeV electrons at $L^* = 5$, 4.5 and 4, respectively. The blue, green, and red bars at the top of Figure 1 mark the intervals of three enhancements of solar wind density.

Xiong Y and Xie L et al.: Non-storm erosion of MeV outer belt electrons

(red line) are plotted in Figure 1d and exhibit a nearly simultaneous sharp decrease with the Van Allen Probes during SWDE1, which did not recover even at the end of three solar wind density enhancements.

The solar wind density, speed, and dynamic pressure, IMF B_z, SYM-H index, and AE index are plotted in Figures 1e–1j, respectively. The solar wind speed was quite low (~300 km/s) during the first two solar wind density enhancements, and then increased up to ~400 km/s in the third enhancement of solar wind density. Due to the relatively low solar wind speed during SWDE1 and SWDE2, the solar wind dynamic pressure only increased by a few nPa. In contrast, during the third solar wind density enhancement, the solar wind dynamic pressure jumped up to ~10 nPa at 18 UT on November 29, due to the sudden increase of solar wind density and relatively high solar wind speed. The IMF B_z was southward in the first half of SWDE1 and began fluctuating during the first half of SWDE2, and then had two southward turnings in the second half of SWDE2. During the last solar wind density enhancement, IMF B_z was almost northward and turned to southward in the middle of SWDE3. The AE index increased during the period of southward IMF B_z, especially in SWDE2 and SWDE3. The SYM-H index remained above −30 nT (marked by the dashed line in Figure 1h) from SWDE1 to SWDE3.

To illustrate the detailed evolution of electron loss processes in different L-shells, we present the PAD (Figures 1k–1m) and normalized PAD (Figures 1n–1p) of 2.1 MeV electrons at L^* = 5.0, 4.5, and 4.0, respectively. During the first solar wind density enhancement, the flux loss and PAD narrowing (due to the more substantial loss of smaller pitch angle electrons) were simultaneously observed at $L^* \geq 4.5$ at 21 UT on November 26. Next, the flux loss process and PAD narrowing signature expanded down to a lower L-shell (L^* = 4.0) at the end of SWDE2. As for the last solar wind density enhancement, the electron fluxes at $L^* \geq 4$ continued to decrease, especially when the solar wind density and dynamic pressure both had a sudden increase at 18 UT on November 29.

3.2 The Evolution of Electron PSD Profiles and Energy-Dependent Narrowing of Electron PAD

To determine the major loss mechanism for the electron flux decrease, we investigate the evolution of electron PSD as a function of L^*. Figure 2c illustrates the electron PSD profile for the first two adiabatic invariants of μ = 1200 MeV/G and K = 0.4 $G^{1/2}R_E$ (corres-
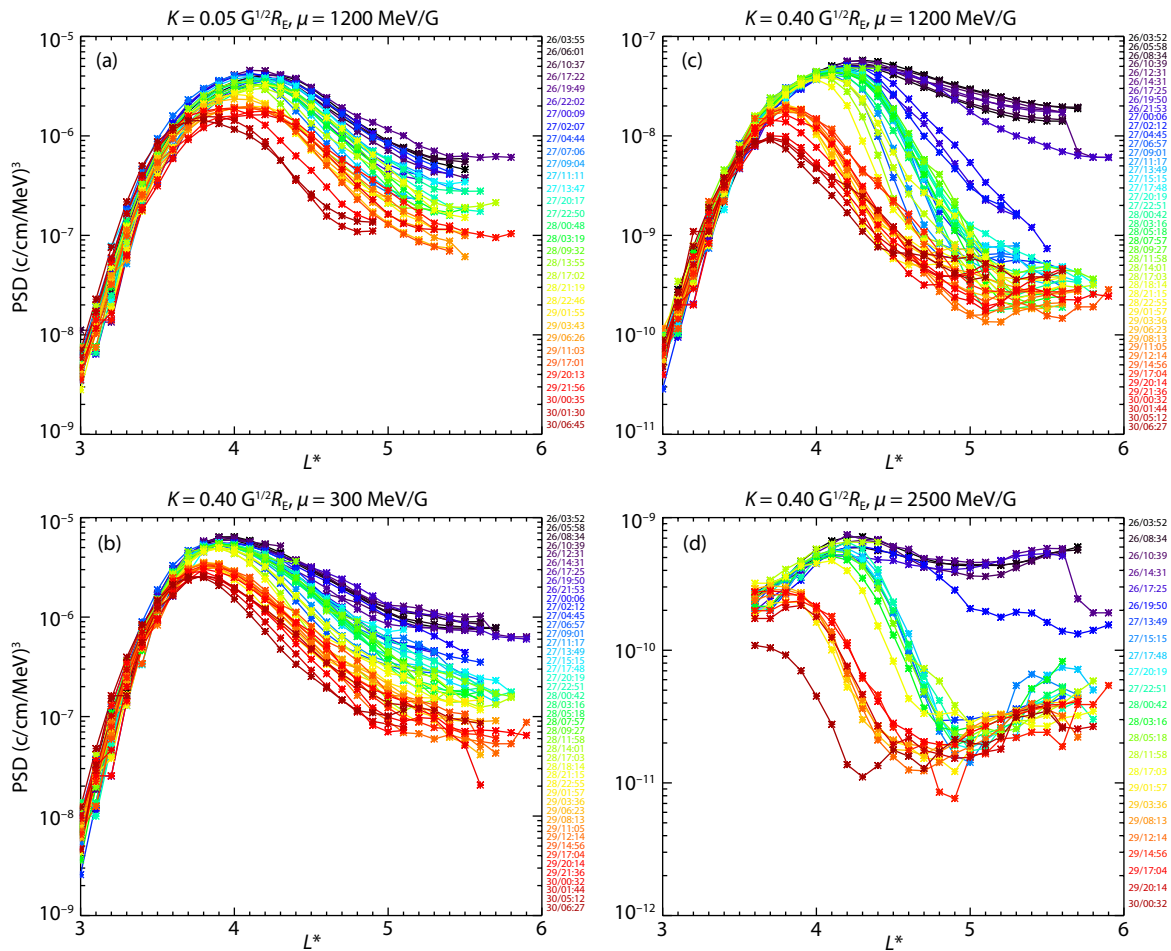

Figure 2. The evolution of electron PSD profiles for four types of electrons: (a) μ = 1200 MeV/G and K = 0.05 $G^{1/2}R_E$ (corresponding to electrons with ~1.6 MeV and ~63 degrees pitch angle at L^* = 4.5); (b) μ=300 MeV/G and K = 0.4 $G^{1/2}R_E$ (corresponding to the electrons with ~1.4 MeV and ~35 degrees pitch angle at L^* = 4.5); (c) μ=1200 MeV/G and K = 0.4 $G^{1/2}R_E$ (corresponding to electrons with ~3.1 MeV and ~35 degrees pitch angle at L^* = 4.5); (d) μ = 2500 MeV/G and K = 0.4 $G^{1/2}R_E$ (corresponding to the electrons with ~4.7 MeV and ~35 degrees pitch angle at L^* = 4.5).

ponding to relativistic electrons of ~3.1 MeV and ~35° pitch angle at $L^* = 4.5$) based on measurements from Van Allen Probes A&B. The time tags of the Van Allen Probes passing through $L^* = 4.5$ during each outbound/inbound are color-coded and labeled at the right side of Figure 2c. During SWDE1, the electron PSDs show a rapid dropout at $L^* > 4.5$, consistent with the outward diffusion dominant loss process. However, during SWDE2, the electron PSDs around $L^* = 4$ and 5 barely changed. Meanwhile, the PSDs at L^* around 4–5 show a dramatic decrease and a local PSD minimum is formed at the end of SWDE2, suggesting that a rapid local loss process occurs (Shprits et al., 2017). During SWDE3, the PSD peak decreases and moves to lower L^* and the PSD at the left side of the peak increases slightly, indicating that radial diffusion may contribute to the PSD loss around $L^* \sim 4$ (Turner et al., 2019).

In comparison with Figure 1b, Figure 2a plots the PSD profiles for electrons with larger pitch angles. The PSD data of these electrons with the first two adiabatic invariants of $\mu = 1200$ MeV/G and $K = 0.05$ $G^{1/2}R_E$ (corresponding to relativistic electrons of ~1.6 MeV and ~63° pitch angle at $L^* = 4.5$) is also based on the measurements from Van Allen Probe-A&B. Since the invariant K is much smaller than in Figure 2c, Van Allen Probes may not have measured those electrons at relatively high latitude. Therefore, the profiles in Figure 2a are less than in Figure 2c. In contrast to the electrons with smaller pitch angles in Figure 2c, the gradual PSD decreases are observed at all L-shells higher than $L^* \sim 4$, implying a dominant loss driven by outward radial diffusion. If we compare Figure 2b–2d with Figure 2c, we can conclude that as the energy increases, localized PSD dips become more evident which is quite consistent with the scenario of EMIC wave scattering loss.

Figure 3 illustrates the PADs (left panels) and normalized PADs (right panels) of electrons with energies from 597 keV up to 4.2 MeV at $L^* = 4.5$. Electron flux decreases are observed in all five channels throughout the entire SWEDs. During SWDE1 and SWDE3, along with the electron flux losses, the electron PADs become narrow. The PADs with higher energies get more concentrated to a 90-degree pitch angle, suggesting that EMIC waves may contribute to the small pitch angle electron losses. In contrast, for SWDE2 a similar energy-dependent pitch angle narrow-

ing is observed, except for 579 keV electrons.

To figure out why there is no evident PAD-narrowing feature in the loss process of 597 keV electron during SWDE2, we estimate that the minimum energy for electrons has resonant interaction with H+ band EMIC waves, as measured by Van Allen Probe-B at $L^* \sim 4.5$ during SWDE2 (shown in Figure 5c). We assume that the EMIC waves are in the L-mode of parallel propagation and that the ion composition is: H+ (77%), He+ (20%), O+ (3%) (Jordanova et al., 2008), then we can use the L-mode dispersion relation in cold plasma theory to calculate the minimum resonant energy for interaction with the observed EMIC waves (Summers and Thorne, 2003). Figure 4 plots the minimum resonant energies for EMIC waves with the power spectrum density > 0.01 nT²/Hz. The lowest E_{min} is ~1.1 MeV, suggesting that the 597 keV and 749 keV electrons cannot have resonant interactions with the observed H* band EMIC waves during SWDE2. Therefore, it is reasonable that there is an evident energy-dependent PAD-narrowing feature for 1097 keV to 4.2 MeV electrons except for 597 keV and 749 keV
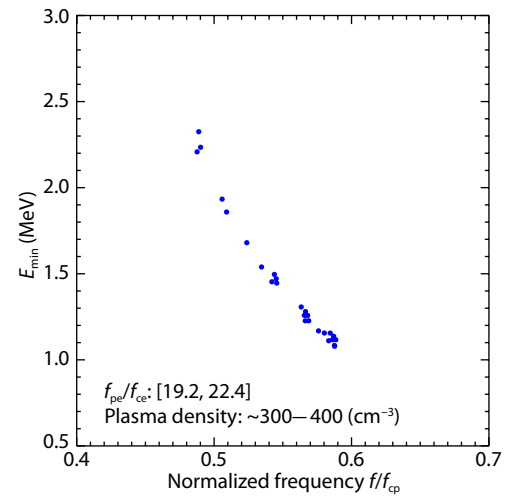

Figure 4. The minimum energy for electrons to have resonant interactions with EMIC waves observed by Van Allen Probe-B at $L^* \sim 4.5$ during SWDE2.
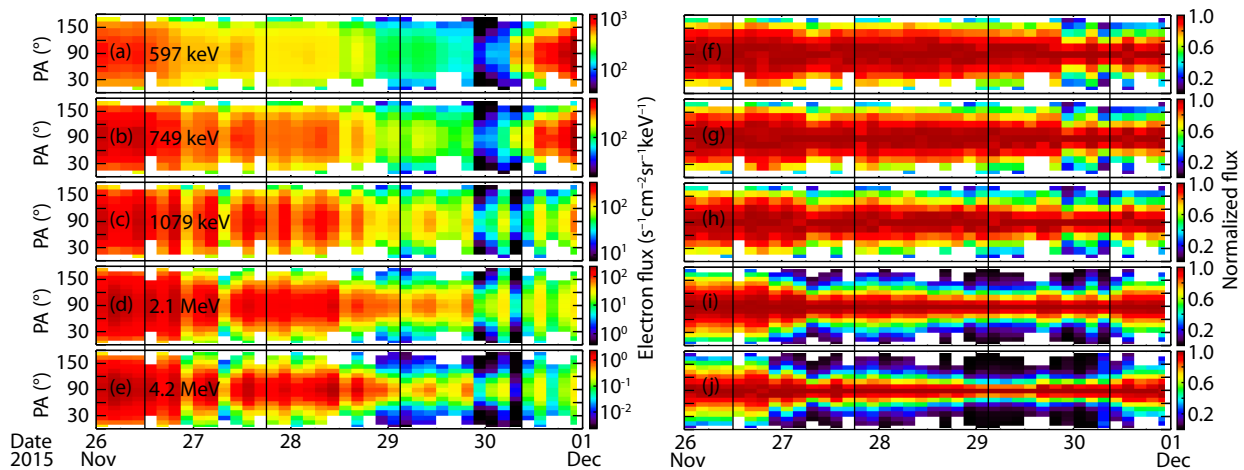

Figure 3. The electron PADs at $L^* = 4.5$. (a–e) the electron PAD with energy from 597 keV up to 4.2 MeV. (f–j) the electron PADs normalized by the flux at 90-degree pitch angles. The vertical black lines mark the boundaries of three solar wind density enhancement intervals.

electrons during SWDE2.

3.3 Inward Extension of EMIC Waves and Electron Precipitation

Since scattering by EMIC waves plays an essential role in the outer belt MeV electron erosion event, it is reasonable to suggest that the inward development of MeV electron loss maybe driven by the inward extension of EMIC waves. Thus, we checked the EMIC wave activity measured by Van Allen Probes and ground magnetometers from CARISMA stations.

Figure 5 shows the EMIC waves observed at different L values during the three SWDE's. Figure 5a illustrates the solar wind density. The dark red and yellow bars on the top of the first panel mark the interval where the EMIC waves were observed by ground stations and Van Allen Probes, respectively (possibly simultaneously). The

black triangles denote the time when Van Allen Probe-A passed $L^* = 4.5$, where the dramatic PSD loss occurred during three SWDEs. Figure 5c plots the magnetic power spectrum density measured by Van Allen Probe A at $L^* \sim 5$ during SWDE1. The white, green, and red dashed curves represent the proton, helium, and oxygen gyrofrequency. Hydrogen band EMIC waves were observed. The remaining four subplots in the left column (Figures 5e, 5h, 5k, and 5n) show the magnetic power spectrum density measured at four ground stations from $L = 4.16$ to 6.71 (where L is calculated using the IGRF model). EMIC waves were measured by two stations at $L = 6.38$ and 6.71 for SWDE1. During the second solar wind density enhancement, as shown by the middle column in Figure 5, EMIC waves occurred at lower L-shells observed by Van Allen Probe-B at $L^* \sim 4.5$. For the ground measurements, EMIC waves were not only observed at two high-L stations (i.e., $L = 6.38$ and 6.71) but also measured by the station at $L = 5.25$. Further, the
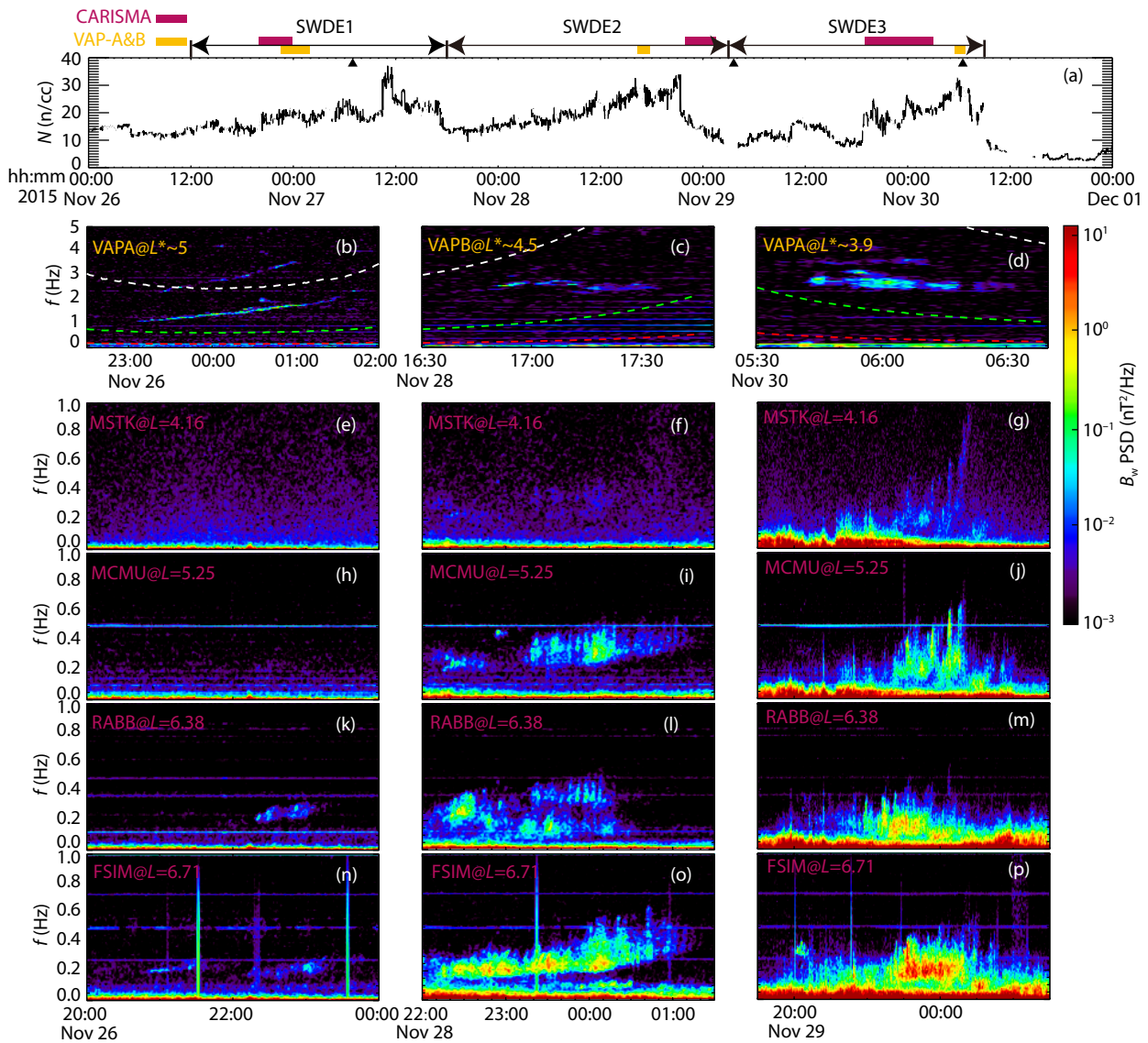

Figure 5. EMIC waves observed at different L values during three solar wind density enhancements. (a) the solar wind density; (b–d) EMIC waves measured by Van Allen Probes during three solar wind density enhancements; (e–p) EMIC waves measured at four CARISMA stations with $L = 4.16$, 5.25, 6.38, and 6.71. The dark red and yellow bars on top of Figure 5 denote the intervals when EMIC waves were observed by ground stations and Van Allen Probes, respectively.

wave strength was much stronger for SWDE2 than was observed during SWDE1. The right column in Figure 5 illustrates EMIC wave distributions at different L-shells during SWDE3; EMIC waves were measured by Van Allen Probe-A (L^* ~3.9) and the ground station (L = 4.16) at lower L-values. This shows that from the first to the third enhancement in solar wind density, the radial distribution of EMIC waves extended accordingly. Specifically, the inner edge of EMIC wave distribution moved from L^* ~5 to L^* ~4 based on in situ Van Allen Probes observations, and from L = 6.38 to L = 4.16 based on ground measurements. The extension of EMIC wave distribution was roughly consistent with the evolution of the MeV electron loss process from L^* = 5 down to L^* = 4, as shown in Figures 1 and 2.

Energetic electron precipitation is a piece of substantial evidence to determine whether EMIC wave scattering plays a role in the loss of energetic electrons. Following the procedure provided by Carson et al. (2013), we survey the energetic electron precipitation during the SWDEs based on measurements by NOAA-15, NOAA-18, and Metop-01. Figure 6a and 6b plot the 30–80 keV proton flux and the > 800 keV electron flux, respectively. The red lines denote the trapped flux, and the blue lines mark the precipitation flux. The green traces are the running average of the precipitation fluxes with an 18 second window (9 data points). The dark vertical line marks the simultaneous sharp increase of proton and electron precipitation fluxes at L ~5.0. Figure 6c depicts all six precipitations recorded by the three NOAA satellites during the entire SWEDs. The black, blue, and red plus signs represent precipitations during SWDE1, SWDE2, and SWDE3, respectively. There is only one precipitation in SWDE1 at L ~5, while there are five precipitations during SWDE2&3. In comparison with SWDE1, we suggest that the precipitation loss is more important during SWDE2&3. The locations where Van Allen Probes measured EMIC waves are plotted in Figure 6d with the same color code. The blue dashed line records the EMIC waves right before the end of SWDE2. The traces of the four ground station footprint where EMIC waves occurred are shown in Figure 6e. The color code is the same as in Figure 6c and 6d. The trend of the inward extension of EMIC waves observed by Van Allen Probes and ground stations from SWDE1 to SWDE2&3 is roughly consistent with inward movements of the precipitation signals. Although the MLT coverage of the precipitations and EMIC waves are not fully overlapped, we suggest that the precipitation loss at L = 4–5 during SWDE2 & 3 may be driven by the inward extension of EMIC waves.

4. Discussions

In section 3.3, we confirm that the inward development of MeV small-pitch-angle electron losses is roughly consistent with the inward extension of EMIC waves, supporting that the electron scattering loss by EMIC waves can account for the outer zone MeV electron erosion during the last two SWDEs. In this section, we try to determine the driving process for the inward extension of EMIC waves. Since EMIC waves generally undergo parallel propagation, the observed EMIC waves at lower L-shells are very likely excited locally.

Figure 7 provides an overview of the background plasma conditions measured by Van Allen Probe-A during the three SWDEs.
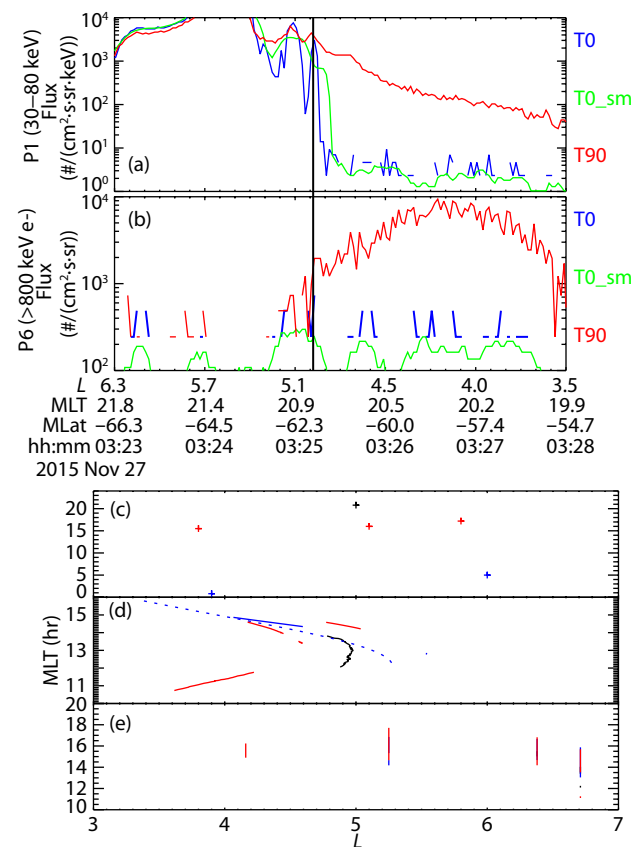

Figure 6. The distribution of precipitation and EMIC waves. (a–b) precipitation example observed by NOAA-18 during SWDE1. (c) the distribution of precipitation throughout the entire SWDEs. (d) the distribution of EMIC waves observed by the Van Allen Probes. (e) the distribution of EMIC waves observed by four ground stations mentioned in Figure 5. The black, blue, and red colors denote the precipitations/EMIC waves measured during SWDE1, SWDE2, and SWDE3, respectively.

Figures 7a–7c plot the solar wind density, IMF B_z, and AE index, respectively. The dark red and yellow bars and black triangles on the top of Figure 7 are the same as Figure 5. The three intervals marked by the vertical black lines correspond to the three outbound orbits of the Van Allen Probe-A close to the EMIC waves they measured. Figure 7d presents the proton PSD multiplied by the proton first adiabatic invariant μ as a function of μ and L^*; for convenience, we only focus on protons with 90° pitch angle. The reason why we use μ*PSD instead of PSD is that it is easier to recognize the radial variations of μ*PSD at different μ-values in the color contour figure. The red dashed lines from top to bottom indicate the μ of protons with constant kinetic energy equal to 30 keV, 10 keV, and 1 keV, respectively. The perpendicular and parallel energy spectra of protons with energies from 0.1 keV to 50 keV are illustrated in Figures 7g and 7j, respectively. The perpendicular protons with 5–10 keV energies could be observed at L^* > 4.0, while the parallel protons with the same energy range could only be observed at L^* > 4.5. There was no evident anisotropy for ~5–10 keV protons, implying that the observed EMIC waves might not be excited locally. Figure 7m shows the high-frequency wave spectrum obtained from the HFR instrument in EM-
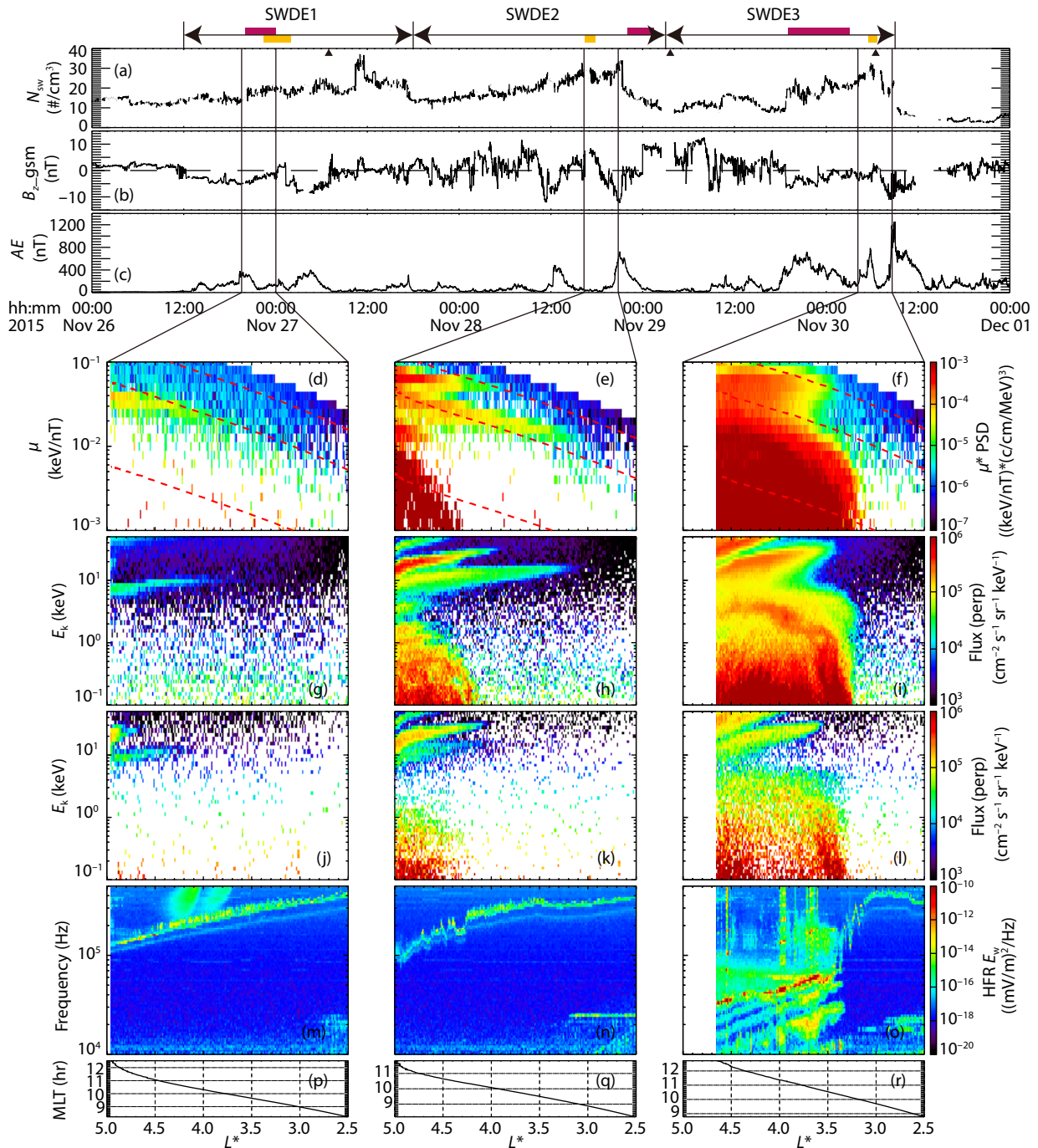
Figure 7. The background plasma conditions measured by Van Allen Probe-A during the three SWDEs. (a−c) solar wind density, IMF B_z, and AE index; (d−f) μ^*PSD as a function of μ and L^*; (g−i) perpendicular energy spectrum of 0.1−50 keV protons; (j−l) parallel energy spectrum of 0.1−50 keV protons; (m−o) HFR electric filed power spectrum density; (p−r) MLT as a function of L^*. The dark red and yellow bars at the top denote the intervals when EMIC waves were observed by ground stations and Van Allen Probes, respectively.

FISIS-A. The banded upper hybrid resonant emission with a frequency higher than 105 Hz indicates that the spacecraft traveled through the plasmasphere (and/or a plasmaspheric plume). Figure 7p illustrates the profiles of MLT versus L^*.

During SWDE2, the protons with μ ~600 keV/nT (corresponding to the protons with energies of 10−30 keV from $L^* = 5$ to $L^* = 4$) penetrated down to $L^* = 4$ (Figure 7e). There was a positive PSD gradient for protons with μ ~600 keV/nT, indicating that those energet-

ic protons may be transported from higher L-shells via the enhanced convection and/or substorm injections. As for the energy spectrum in the perpendicular direction (shown in Figure 7h), there was a three-banded structure (also known as the "multi-nose" structure (Ferradas et al., 2016)) for >10 keV protons. The evident anisotropic nose structure may provide free energy to excite EMIC waves at $L^* > 4$ (Zhang JC et al., 2014; Fok et al., 2016).

During SWDE3, the protons with μ ~600 keV/nT penetrated to $L^* =$

3.5. The anisotropic energetic protons (>10 keV) extended down to $L^* = 3.5$, while anisotropic warm protons (100 eV to 1 keV) penetrated to $L^* = 3.3$. As shown in Figure 7o, the frequency of the upper hybrid resonant emission had a dramatic decrease around $L^* = 3.3$, indicating that the plasmapause location was near $L^* = 3.3$. The overlap of the anisotropic energetic and warm protons may both contribute to the excitation of the EMIC waves at such lower L-shells (Teng SC et al., 2019). The inward penetration of the energetic protons from $L^* = 4.5$ during SWDE1 to $L^* = 3.5$ during SWDE3 is roughly consistent with the inward extension of EMIC waves shown in Figure 3.

During SWDE1&2, the solar wind dynamic pressure increased gradually along with the enhancements of the solar wind density, suggesting that electron losses due to the magnetopause shadowing effect may be less important than EMIC wave-induced scattering loss. During SWDE3, the solar wind dynamic pressure had a sudden increase at 18 UT on November 29.

It is challenging to determine the relationship between high solar wind density and the loss of MeV electrons in the outer radiation belt. We tried to resolve this question based on observations from Van Allen Probes and ground stations, proposing that the inward penetration of anisotropic energetic protons from the plasma sheet due to enhanced convection and/or substorm injections can lead to the inward extension of EMIC waves. They subsequently can cause electron scattering loss from high L-shells ($L^* = 5.5$) down to lower L-shells ($L^* < 4$) which is around the heart of the outer radiation belt, leading to efficient precipitation losses. The impacts of high solar wind density on energetic proton dynamics in the inner magnetosphere is still an open question requiring further study.

5. Conclusions

In this paper, we reported an unusual non-storm MeV electron flux loss event during three successive enhancements of solar wind density measured by Van Allen Probes on November 27−30, 2015. Our principal conclusions are summarized as follows:

(1) The electron flux decrease along with energy-dependent PAD narrowing (i.e., higher energy electrons manifest a narrower PAD) was initially observed at higher L-shells ($L^* \sim 5.5$) and then developed down to lower L-shells ($L^* < 4.0$).

(2) The PSD losses of electrons with small pitch angles at $L^* > 4.5$ are mainly due to outward radial diffusion during SWDE1. Decreases of electron PSD moving down to $L^* = 4$ at the end of SWDE2 are dominated by EMIC wave scattering loss, and further reached the region of $L^* < 4$ during SWDE3. This may result from the combined effect of radial diffusion and EMIC wave scattering. Further, for electrons with large pitch angles, the PSD loss is mainly controlled by outward radial diffusion throughout the entirety of SWDEs.

(3) From the first to third enhancements of solar wind density, the inner edge of EMIC wave activity observed by Van Allen Probes and by ground stations moved respectively from $L^* = 5$ to $L^* = 3.9$, and from $L = 6.38$ to $L = 4.16$, respectively. This is consistent with the penetration of anisotropic energetic protons from $L^* = 4.5$ to

$L^* = 3.5$, suggesting that the inward extension of EMIC waves may be driven by inward injection of the anisotropic energetic protons from the dense plasma sheet.

In contrast to many previous studies that focused on the impacts of solar wind speed and solar wind dynamic pressure on the dynamics of outer radiation belt electrons, our results suggest that enhanced solar wind density might act as an external driver of the outer zone MeV electron loss process. However, the physical mechanism underlying the relationship between high solar wind density and outer zone MeV electron loss due to EMIC wave scattering remains unknown.

References

Anderson, B. J., and Hamilton, D. C. (1993). Electromagnetic ion cyclotron waves stimulated by modest magnetospheric compressions. *J. Geophys. Res.: Space Phys.*, *98*(A7), 11369–11382. https://doi.org/10.1029/93JA00605

Aseev, N. A., Shprits, Y. Y., Drozdov, A. Y., Kellerman, A. C., Usanova, M. E., Wang, D., and Zhelavskaya, I. S. (2017). Signatures of ultrarelativistic electron loss in the heart of the outer radiation belt measured by van Allen Probes. *J. Geophys. Res.: Space Phys.*, *122*(10), 10102–10111. https://doi.org/10.1002/2017JA024485

Baker, D. N., Kanekal, S. G., Hoxie, V. C., Batiste, S., Bolton, M., Li, X., Elkington, S. R., Monk, S., Reukauf, R., … Cervelli, B. (2013). The Relativistic Electron-Proton Telescope (REPT) instrument on board the Radiation Belt Storm Probes (RBSP) spacecraft: Characterization of Earth's radiation belt high-energy particle populations. *Space Sci. Rev.*, *179*(1-4), 337–381. https://doi.org/10.1007/s11214-012-9950-9

Balikhin, M. A., Boynton, R. J., Walker, S. N., Borovsky, J. E., Billings, S. A., & Wei, H. L. (2011). Using the NARMAX approach to model the evolution of energetic electrons fluxes at geostationary orbit. *Geophysical Research Letters*, *38*(18), L18105. https://doi.org/10.1029/2011gl048980

Blake, J. B., Baker, D. N., Turner, N., Ogilvie, K. W., and Lepping, R. P. (1997). Correlation of changes in the outer-zone relativistic-electron population with upstream solar wind and magnetic field measurements. *Geophys. Res. Lett.*, *24*(8), 927–929. https://doi.org/10.1029/97GL00859

Blake, J. B., Carranza, P. A., Claudepierre, S. G., Clemmons, J. H., Crain Jr, W. R., Dotan, Y., Fennell, J. F., Fuentes, F. H., Galvan, R. M., … Zakrzewski, M. P. (2013). The Magnetic Electron Ion Spectrometer (MAGEIS) instruments aboard the Radiation Belt Storm Probes (RBSP) spacecraft. *Space Sci. Rev.*, *179*(1-4), 383–421. https://doi.org/10.1007/s11214-013-9991-8

Borovsky, J. E., Thomsen, M. F., and Elphic, R. C. (1998). The driving of the plasma sheet by the solar wind. *J. Geophys. Res.: Space Phys.*, *103*(A8), 17617–17639. https://doi.org/10.1029/97JA02986

Borovsky, J. E., and Denton, M. H. (2009). Relativistic-electron dropouts and recovery: A superposed epoch study of the magnetosphere and the solar

wind. *J. Geophys. Res.: Space Phys.*, *114*(A2), A02201. https://doi.org/10.1029/2008JA013128

Borovsky, J. E., and Denton, M. H. (2014). Exploring the cross correlations and autocorrelations of the ULF indices and incorporating the ULF indices into the systems science of the solar wind-driven magnetosphere. *J. Geophys. Res.: Space Phys.*, *119*(6), 4307–4334. https://doi.org/10.1002/2014JA019876

Borovsky, J. E., and Shprits, Y. Y. (2017). Is the Dst index sufficient to define all geospace storms?. *J. Geophys. Res.: Space Phys.*, *122*(11), 11543–11547. https://doi.org/10.1002/2017JA024679

Boynton, R. J., Balikhin M. A., Billings, S. A., Reeves, G. D., Ganushkina, N., Gedalin, M., Amariutei, O. A., Borovsky, J. E., Walker, S. N. (2013). The analysis of electron fluxes at geosynchronous orbit employing a NARMAX approach. *Journal of Geophysical Research:Space Physics*, *118*(4), 1500–1513. https://doi.org/10.1002/jgra.50192

Breneman, A. W., Crew, A., Sample, J., Klumpar, D., Johnson, A., Agapitov, O., Shumko, M., Turner, D. L., Santolik, O., … Kletzing, C. A. (2017). Observations directly linking relativistic electron microbursts to whistler mode chorus: Van Allen Probes and FIREBIRD II. *Geophys. Res. Lett.*, *44*(22), 11265–11272. https://doi.org/10.1002/2017GL075001

Carson, B. R., Rodger, C. J., and Clilverd, M. A. (2013). POES satellite observations of EMIC-wave driven relativistic electron precipitation during 1998-2010. *J. Geophys. Res.: Space Phys.*, *118*(1), 232–243. https://doi.org/10.1029/2012JA017998

Chen, L. J., Thorne, R. M., Jordanova, V. K., Wang, C. P., Gkioulidou, M., Lyons, L., and Horne, R. B. (2010). Global simulation of EMIC wave excitation during the 21 April 2001 storm from coupled RCM-RAM-HOTRAY modeling. *J. Geophys. Res.: Space Phys.*, *115*(A7), A07209. https://doi.org/10.1029/2009JA015075

Engebretson, M. J., Peterson, W. K., Posch, J. L., Klatt, M. R., Anderson, B. J., Russell, C. T., Singer, H. J., Arnoldy, R. L., and Fukunishi, H. (2002). Observations of two types of Pc 1-2 pulsations in the outer dayside magnetosphere. *J. Geophys. Res.: Space Phys.*, *107*(A12), 1451. https://doi.org/10.1029/2001JA000198

Engebretson, M. J., Posch, J. L., Braun, D. J., Li, W., Ma, Q., Kellerman, A. C., Huang, C. L., Kanekal, S. G., Kletzing, C. A., … Baker, D. N. (2018). EMIC wave events during the four GEM QARBM challenge intervals. *J. Geophys. Res.: Space Phys.*, *123*(8), 6394–6423. https://doi.org/10.1029/2018JA025505

Evans, D. S., and M. S. Greer (2004), Polar orbiting Environmental Satellite Space Experiment Monitor-2: Instrument descriptions and archive data documentation, NOAA Technical Memorandum version 1.3. NOAA Space Environment Center, Boulder, Colo.

Ferradas, C. P., Zhang, J. C., Spence, H. E., Kistler, L. M., Larsen, B. A., Reeves, G., Skoug, R., and Funsten, H. (2016). Ion nose spectral structures observed by the Van Allen Probes. *J. Geophys. Res. Space Phys.*, *121*(12), 12025–12046. https://doi.org/10.1002/2016JA022942

Fok, M. C., Khazanov, G. V., Krivorutsky, E. N., and Glocer, A. (2016). Convective growth of electromagnetic ion cyclotron waves from realistic ring current ion distributions. *J. Geophys. Res.: Space Phys.*, *121*(11), 10966–10977. https://doi.org/10.1002/2016JA022964

Funsten, H. O., Skoug, R. M., Guthrie, A. A., MacDonald, E. A., Baldonado, J. R., Harper, R. W., Henderson, K. C., Kihara, K. H., Lake, J. E., ... Chen J. (2013). Helium, Oxygen, Proton, and Electron (HOPE) mass spectrometer for the Radiation Belt Storm Probes mission. *Space Sci. Rev.*, *179*, 423–484. https://doi.org/10.1007/s11214-013-9968-7

Green, J. (2013). MEPED telescope data processing theoretical basis document version 1.0, NOAA Technical Memorandum, version 1.0. Available at http://www.ngdc.noaa.gov/stp/satellite/poes/documentation.html.

Hudson, M. K., Baker, D. N., Goldstein, J., Kress, B. T., Paral, J., Toffoletto, F. R., and Wiltberger, M. (2014). Simulated magnetopause losses and Van Allen Probe flux dropouts. *Geophys. Res. Lett.*, *41*(4), 1113–1118. https://doi.org/10.1002/2014GL059222

Jordanova, V. K., Albert, J., and Miyoshi, Y. (2008). Relativistic electron precipitation by EMIC waves from self-consistent global simulations. *J. Geophys. Res.: Space Phys.*, *113*(A3), A00A10. https://doi.org/10.1029/2008JA013239

Katsavrias, C., Daglis, I. A., Turner, D. L., Sandberg, I., Papadimitriou, C., Georgiou, M., and Balasis, G. (2015). Nonstorm loss of relativistic electrons in the outer radiation belt. *Geophys. Res. Lett.*, *42*(24), 10521–10530. https://doi.org/10.1002/2015GL066773

Kersten, T., Horne, R. B., Glauert, S. A., Meredith, N. P., Fraser, B. J., and Grew, R. S. (2014). Electron losses from the radiation belts caused by EMIC waves. *J. Geophys. Res.: Space Phys.*, *119*(11), 8820–8837. https://doi.org/10.1002/2014JA020366

Kim, H. J., and Chan, A. A. (1997). Fully adiabatic changes in storm time relativistic electron fluxes. *J. Geophys. Res.: Space Phys.*, *102*(A10), 22107–22116. https://doi.org/10.1029/97JA01814

Kletzing, C. A., Kurth, W. S., Acuna, M., MacDowall, R. J., Torbert, R. B., Averkamp, T., Bodet, D., Bounds, S. R., Chutter, M., ... Tyler, J. (2013). The Electric and Magnetic Field Instrument Suite and Integrated Science (EMFISIS) on RBSP. *Space Sci. Rev.*, *179*(1-4), 127–181. https://doi.org/10.1007/s11214-013-9993-6

Li, W., Shprits, Y. Y., and Thorne, R. M. (2007). Dynamic evolution of energetic outer zone electrons due to wave-particle interactions during storms. *J. Geophys. Res.: Space Phys.*, *112*(A10), A10220. https://doi.org/10.1029/2007JA012368

Li, X. L., Temerin, M., Baker, D. N., Reeves, G. D., and Larson, D. (2001). Quantitative prediction of radiation belt electrons at geostationary orbit based on solar wind measurements. *Geophys. Res. Lett.*, *28*(9), 1887–1890. https://doi.org/10.1029/2000GL012681

Liu, N. G., Su, Z. P., Gao, Z. L., Zheng, H. N., Wang, Y. M., and Wang, S. (2020). Can solar wind decompressive discontinuities suppress magnetospheric electromagnetic ion cyclotron waves associated with fresh proton injections?. *Geophys. Res. Lett.*, *47*(17), e2020GL090296. https://doi.org/10.1029/2020GL090296

Lorentzen, K. R., Blake, J. B., Inan, U. S., and Bortnik, J. (2001). Observations of relativistic electron microbursts in association with VLF chorus. *Journal of Geophysical Research*, *106*(A4), 6017–6027. https://doi.org/10.1029/2000JA003018

Loto'aniu, T. M., Mann, I. R., Ozeke, L. G., Chan, A. A., Dent, Z. C., and Milling, D. K. (2006). Radial diffusion of relativistic electrons into the radiation belt slot region during the 2003 Halloween geomagnetic storms. *J. Geophys. Res.: Space Phys.*, *111*(A4), A04218. https://doi.org/10.1029/2005JA011355

Lyatsky, W., and Khazanov, G. V. (2007). Prediction of geomagnetic activity and key parameters in high-latitude ionosphere–basic elements. NASA/TP-2007-215079, Washington, DC: NASA, 29.

Lyatsky, W., and Khazanov, G. V. (2008). Effect of solar wind density on relativistic electrons at geosynchronous orbit. *Geophys. Res. Lett.*, *35*(3), L03109. https://doi.org/10.1029/2007GL032524

Ma, X., Xiang, Z., Ni, B. B., Fu, S., Cao, X., Hua, M., Guo, D. Y., Guo, Y. J., Gu, X. D., Liu, Z. Y. and Zhu, Q. (2020). On the loss mechanisms of radiation belt electron dropouts during the 12 September 2014 geomagnetic storm. *Earth Planet. Phys.*, *4*(6), 598–610. https://doi.org/10.26464/epp2020060

Meredith, N. P., Horne, R. B., Thorne, R. M., Summers, D., and Anderson, R. R. (2004). Substorm dependence of plasmaspheric hiss. *J. Geophys. Res.: Space Phys.*, *109*(A9), A06209. https://doi.org/10.1029/2004JA010387

Millan, R. M., and Thorne, R. M. (2007). Review of radiation belt relativistic electron losses. *J. Atmos. Sol. Terr. Phys.*, *69*(3), 362–377. https://doi.org/10.1016/j.jastp.2006.06.019

Morley, S. K., Friedel, R. H. W., Cayton, T. E., and Noveroske, E. (2010). A rapid, global and prolonged electron radiation belt dropout observed with the Global Positioning System constellation. *Geophys. Res. Lett.*, *37*(6), L06102. https://doi.org/10.1029/2010GL042772

Mozer, F. S., Agapitov, O. V., Hull, A., Lejosne, S., and Vasko, I. Y. (2017). Pulsating auroras produced by interactions of electrons and time domain structures. *J. Geophys. Res.: Space Phys.*, *122*(8), 8604–8616. https://doi.org/10.1029/2017JA024223

Mauk, B. H., Fox, N. J., Kanekal, S. G., Kessel, R. L., Sibeck, D. G., and Ukhorskiy, A. (2013). Science objectives and rationale for the radiation belt storm probes mission. *Space Sci. Rev.*, *179*(1–4), 3–27. https://doi.org/10.1007/s11214-012-9908-y

Ni, B. B., Shprits, Y. Y., Friedel, R., H. W., Thorne, R. M., Daae, M., and Chen, Y. (2013). Responses of Earth's radiation belts to solar wind dynamic pressure variations in 2002 analyzed using multisatellite data and Kalman filtering. *J. Geophys. Res.: Space Phys.*, *118*(7), 4400–4414. https://doi.org/10.1002/jgra.50437

Reeves, G. D., Morley, S. K., Friedel, R. H. W., Henderson, M. G., Cayton, T. E., Cunningham, G., Blake, J. B., Christensen, R. A., and Thomsen, D. (2011). On the relationship between relativistic electron flux and solar wind velocity: Paulikas and Blake revisited. *J. Geophys. Res.: Space Phys.*, *116*(A2), A02213. https://doi.org/10.1029/2010JA015735

Shprits, Y. Y., Thorne, R. M., Friedel, R., Reeves, G. D., Fennell, J., Baker, D. N., and Kanekal, S. G. (2006). Outward radial diffusion driven by losses at magnetopause. *J. Geophys. Res.: Space Phys.*, *111*(A11), A11214. https://doi.org/10.1029/2006JA011657

Shprits, Y. Y., Kellerman, A., Aseev, N., Drozdov, A. Y., and Michaelis, I. (2017). Multi-MeV electron loss in the heart of the radiation belts. *Geophys. Res. Lett.*, *44*(3), 1204–1209. https://doi.org/10.1002/2016GL072258

Su, Z. P., Xiao, F. L., Zheng, H. N., and Wang, S. (2011). CRRES observation and STEERB simulation of the 9 October 1990 electron radiation belt dropout event. *Geophys. Res. Lett.*, *38*(6), L06106. https://doi.org/10.1029/2011GL046873

Su, Z. P., Xiao, F. L., Zheng, H. N., He, Z. G., Zhu, H., Zhang, M., Shen, C., Wang, Y. M., Wang, S., … Hospodarsky, G. B. (2014). Nonstorm time dynamics of electron radiation belts observed by the Van Allen Probes. *Geophys. Res. Lett.*, *41*(2), 229–235. https://doi.org/10.1002/2013GL058912

Su, Z. P., Zhu, H., Xiao, F. L., Zong, Q. G., Zhou, X. Z., Zheng, H. N., Wang, Y. M., Wang, S., Hao, Y. X., … Wygant, J. R. (2015). Ultra-low-frequency wave-driven diffusion of radiation belt relativistic electrons. *Nat. Commun.*, *6*, 10096. https://doi.org/10.1038/ncomms10096

Su, Z. P., Gao, Z. L., Zhu, H., Li, W., Zheng, H. N., Wang, Y. M., Wang, S., Spence, H. E., Reeves, G. D., … Wygant, J. R. (2016). Nonstorm time dropout of radiation belt electron fluxes on 24 September 2013. *J. Geophys. Res.: Space Phys.*, *121*(7), 6400–6416. https://doi.org/10.1002/2016JA022546

Summers, D., and Thorne, R. M. (2003). Relativistic electron pitch-angle scattering by electromagnetic ion cyclotron waves during geomagnetic storms. *J. Geophys. Res.: Space Phys.*, *108*(A4), 1143. https://doi.org/10.1029/2002JA009489

Teng, S. C., Li, W., Tao, X., Ma, Q. L., Wu, Y., Capannolo, L., Shen, X. C., and Gan, L. Z. (2019). Generation and characteristics of unusual high frequency EMIC waves. *Geophys. Res. Lett.*, *46*(24), 14230–14238. https://doi.org/10.1029/2019GL085220

Tu, W. C., Li, W., Albert, J. M., and Morley, S. K. (2019). Quantitative assessment of radiation belt modeling. *J. Geophys. Res.: Space Phys.*, *124*(2), 898–904. https://doi.org/10.1029/2018JA026414

Turner, D. L., Shprits, Y., Hartinger, M., and Angelopoulos, V. (2012). Explaining sudden losses of outer radiation belt electrons during geomagnetic storms. *Nat. Phys.*, *8*(3), 208–212. https://doi.org/10.1038/nphys2185

Turner, D. L., Kilpua, E. K. J., Hietala, H., Claudepierre, S. G., O'Brien, T. P., Fennell, J. F., Blake, J. B., Jaynes, A. N., Kanekal, S., … Reeves, G. D. (2019). The response of Earth's electron radiation belts to geomagnetic storms: Statistics from the Van Allen Probes era including effects from different storm drivers. *J. Geophys. Res.: Space Phys.*, *124*(2), 1013–1034. https://doi.org/10.1029/2018JA026066

Usanova, M. E., Mann, I. R., Rae, I. J., Kale, Z. C., Angelopoulos, V., Bonnell, J. W., Glassmeier, K. H., Auster, H. U., and Singer, H. J. (2008). Multipoint observations of magnetospheric compression-related EMIC Pc1 waves by THEMIS and CARISMA. *Geophys. Res. Lett.*, *35*(17), L17S25. https://doi.org/10.1029/2008GL034458

Usanova, M. E., Drozdov, A., Orlova, K., Mann, I. R., Shprits, Y., Robertson, M. T., Turner, D. L., Milling, D. K., Kale, A., … Wygant, J. (2014). Effect of EMIC waves on relativistic and ultrarelativistic electron populations: Ground-based and Van Allen Probes observations. *Geophys. Res. Lett.*, *41*(5), 1375–1381. https://doi.org/10.1002/2013GL059024

Vampola, A. L. (1998). Outer zone energetic electron environment update, in Proceedings of the Conference on the High Energy Radiation Background in Space, pp. 128–136, Inst. of Electr. and Electr. Eng., New York.

Wang, D. D., Shprits, Y. Y., Zhelavskaya, I. S., Effenberger, F., Castillo, A. M., Drozdov, A. Y., Aseev, N. A., and Cervantes, S. (2020). The effect of plasma boundaries on the dynamic evolution of relativistic radiation belt electrons. *J. Geophys. Res.: Space Phys.*, *125*(5), e2019JA027422. https://doi.org/10.1029/2019JA027422

Xiang, Z., Tu, W. C., Li, X. L., Ni, B. B., Morley, S. K., and Baker, D. N. (2017). Understanding the mechanisms of radiation belt dropouts observed by Van Allen Probes. *J. Geophys. Res.: Space Phys.*, *122*(10), 9858–9879. https://doi.org/10.1002/2017JA024487

Xiang, Z., Tu, W. C., Ni, B. B., Henderson, M. G., and Cao, X. (2018). A statistical survey of radiation belt dropouts observed by Van Allen Probes. *Geophys. Res. Lett.*, *45*(16), 8035–8043. https://doi.org/10.1029/2018GL078907

Xiong, Y., Xie, L., Pu, Z. Y., Fu, S. Y., Chen, L. J., Ni, B. B., Li, W., Li, J. X., Guo, R. L., and Parks, G. K. (2015). Responses of relativistic electron fluxes in the outer radiation belt to geomagnetic storms. *J. Geophys. Res.: Space Phys.*, *120*(11), 9513–9523. https://doi.org/10.1002/2015JA021440

Zhang, J. C., Saikin, A. A., Kistler, L. M., Smith, C. W., Spence, H. E., Mouikis, C. G., Torbert, R. B., Larsen, B. A., Reeves, G. D., … Jordanova, V. K. (2014). Excitation of EMIC waves detected by the Van Allen Probes on 28 April 2013. *Geophys. Res. Lett.*, *41*(12), 4101–4108. https://doi.org/10.1002/2014GL060621